ROYAL SOCIETY
OF CHEMISTRY

EDGE ARTICLE

Check for updates

Suppressing nonradiative decay *via* molecular configuration control in Cu(ı)−halide clusters enables the fabrication of highly efficient green and green-sensitized blue OLEDs

Xiao Li,[abc] Sai Guo,[abc] Xin Liu,[abc] Yu-Fu Sun,[abc] Dong-Hai Zhang,[abc] Hui Yang,[abc] Jia-Min Lu*[abc] and Xu-Lin Chen [ID] *[abc]

Copper(ı) complexes are cost-effective and eco-friendly emitters, yet their device applications are hindered by broad emission, by limited film-forming ability, and especially by severe excited-state distortions that typically lead to low emission efficiency in the film state. Herein, to address these challenges, we propose a structural design strategy for highly efficient and sublimable copper(ı)-bromide clusters by simultaneously incorporating donor−acceptor bisphosphine ligands and introducing *ortho*-methyl substitution. This design effectively suppresses intrinsic nonradiative decay by modulating the excited-state geometry, thereby achieving an exceptionally high photoluminescence quantum yield of 99% in doped films. Vacuum-deposited organic light-emitting diodes (OLEDs) using the optimized cluster [dtpb-Ac]$_2$Cu$_2$Br$_2$ as the terminal emitter achieve efficient green emission with a maximum external quantum efficiency (EQE) of 25.1%. Notably, an innovative strategy exploits the intrinsically broad emission of the copper(ı)-bromine cluster to sensitize the deep-blue MR-TADF emitter *ν*-DABNA, achieving high-efficiency green-sensitized blue OLEDs with a maximum EQE of 28.7% and Commission Internationale de l'Eclairage (CIE) coordinates of (0.15, 0.19). As either a green dopant or a sensitizer, the device performance ranks among the best reported for copper(ı)-based OLEDs. The current study presents promising molecular design and sensitization strategies to address the key challenges in developing high-performance copper(ı)-based OLEDs.

Introduction

Organic light-emitting diodes (OLEDs) have been developed as a leading display technology. In the pursuit of high-performance OLEDs, luminescent materials that comprise emitting layers play a key role and have garnered significant attention. Phosphorescent and thermally activated delayed fluorescence (TADF) materials are the two most promising OLED emitters due to their potential for high exciton utilization efficiency (EUE).[1] Phosphorescent platinum-group metal complexes have achieved great success in fabricating green and red pixels for commercial OLEDs. However, these phosphors suffer from high costs and face challenges in achieving high-

efficiency blue phosphorescence due to the intrinsic non-radiative metal-centered dd* states.[2] Multiresonance (MR) TADF molecules featuring mutually *ortho*-positioned boron and nitrogen atoms have emerged as ideal terminal emitters for highly efficient narrowband electroluminescence (EL),[3] assisted by appropriate phosphorescence or TADF sensitizers for triplet harvesting.[4] In these sensitization strategies, a high-performance sensitizer with efficient and rapid triplet-harvesting capability and good spectral overlap with the terminal emitter is essential. In particular, to sensitize deep-blue emitters, the sensitizers should typically be blue-emitting to enable effective Förster resonance energy transfer (FRET) and inhibit back energy transfer.[5] However, the pursuit of ideal blue sensitizers encounters significant challenges due to the stringent molecular design principles required.

Copper(ı) complexes have been extensively investigated as photoluminescence (PL) and EL materials due to their cost-effectiveness, structural diversity, rich photophysical properties, and triplet-harvesting capacity.[6] Owing to the low oxidation potential of the Cu$^+$ ion, the lowest-energy optical transitions in most copper(ı) complexes are mainly characterized by metal-to-ligand charge transfer (MLCT). The MLCT transitions in

[a] State Key Laboratory of Structural Chemistry, Fujian Institute of Research on the Structure of Matter, Chinese Academy of Sciences, Fuzhou, Fujian 350002, China. E-mail: xlchem@fjirsm.ac.cn

[b] Clinical Research Institute, The First Affiliated Hospital of Xiamen University, School of Medicine Xiamen University, Xiamen, Fujian 361003, China. E-mail: lujiamin@xmu.edu.cn

[c] Xiamen Key Laboratory of Rare Earth Photoelectric Functional Materials, Xiamen Institute of Rare Earth Materials, Chinese Academy of Sciences, Xiamen, Fujian 361021, China

copper(I) complexes engender small singlet-triplet energy splitting (ΔE_{ST}), thereby imparting TADF characteristics.[7] However, these MLCT transitions are associated with large reorganization energies and oxidation at the d^{10} metal centre, which not only increase nonradiative decay rates (especially in non-rigid matrices) *via* Jahn–Teller distortion but also lead to broad emission spectra.[8] As a result, most copper(I) complexes exhibit low emission efficiencies and broad emission spectra in films, making them unsuitable as terminal emitters for fabricating efficient and high color-purity OLEDs. Moreover, the fully filled 3d orbitals of copper(I) complexes are energetically high. Although nonradiative dd* states do not exist as in platinum-group metal complexes, the high-level 3d orbitals in copper(I) complexes inevitably result in relatively low-energy MLCT states, presenting a formidable challenge in achieving blue emission, let alone deep-blue emission.[7,9] The EL applications of copper(I) complexes are significantly limited by the aforementioned characteristics of their excited states. Among copper(I) complexes, copper(I)-halide clusters have captured researchers' attention due to their diverse structural and photophysical properties.[10] The involvement of halide ligands in the lowest excited states has been shown to facilitate intersystem crossing (ISC), reduce excited-state distortions, and prevent photothermal decomposition in copper(I)-halide clusters.[11] However, copper(I)-halide clusters share the same limitations as other copper(I) complexes, including undesired rapid nonradiative decay, broad emission spectra, and the challenge of achieving blue emission.[12] The rapid nonradiative decays of intrinsic (metal plus halide)-to-ligand charge transfer [(M + X) LCT] and cluster-centered triplet states (^{3}CC) account for the low emission efficiencies observed in most reported copper(I)-halide clusters in solutions and films.[13] Xu and coworkers recently reported that incorporating electron-donating groups into bidentate phosphine ligands is an effective strategy to reduce the population of nonradiative ^{3}CC states in the Cu_4I_4 cores.[14] Apart from their limitations in photoluminescence, many copper(I)-halide clusters are insoluble in common solvents and unstable during sublimation, rendering them impractical for use in fabricating EL devices. Despite some advancements, designing copper(I)-halide clusters for the construction of highly efficient OLEDs, particularly blue devices, based on a deep understanding of the structure–property relationships remains challenging.

Here, we designed and investigated two copper(I)-bromine clusters, $[dppb-Ac]_2Cu_2Br_2$ and $[dtpb-Ac]_2Cu_2Br_2$, supported by bisphosphine ligands (dppb-Ac and dtpb-Ac) featuring similar donor (D)-acceptor (A) configurations (Fig. 1). Compared with the previously reported copper(I)-bromine cluster coordinated by the commercially available bisphosphine ligand dppb, incorporation of a dimethylacridine unit into the dppb ligand effectively suppresses dissociation of the ligand from the complex in solution (Fig. S15). The further introduction of *ortho*-methyl groups on the bisphosphine ligand dppb-AC significantly affected the molecular configuration, transforming the Cu_2Br_2 core from a "butterfly" shape to a planar parallelogram shape, accompanied by a marked decrease in intramolecular Cu–Cu interaction. Compared with those in
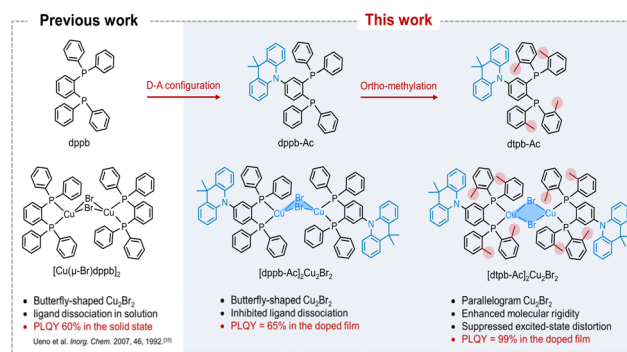

Fig. 1 Molecular design strategy and chemical structures.

$[dppb-Ac]_2Cu_2Br_2$, the contribution of (M + X)LCT decreased while the contribution of intramolecular charge transfer (ILCT) increased in the emissive state (S_1) of $[dtpb-Ac]_2Cu_2Br_2$. As a result, the distortion and nonradiative decay of the S_1 state of $[dtpb-Ac]_2Cu_2Br_2$ are significantly suppressed. $[dtpb-Ac]_2Cu_2Br_2$ in doped films exhibits high PLQYs of up to 99%, which is much higher than the corresponding PLQY of 65% observed for $[dppb-Ac]_2Cu_2Br_2$. The doped OLEDs utilizing $[dtpb-Ac]_2Cu_2Br_2$ as the terminal emitter displayed bright green emission with maximum external quantum efficiencies (EQEs) reaching 25.1% and corresponding FWHMs exceeding 95 nm. Notably, thanks to the high efficiency and broad emission of $[dtpb-Ac]_2Cu_2Br_2$, highly efficient green-sensitized deep-blue OLEDs were fabricated by employing the green-emitting $[dtpb-Ac]_2Cu_2Br_2$ as the sensitizer for the blue MR-TADF emitter ν-DABNA, achieving a maximum EQE of 28.7% and corresponding CIE coordinates of (0.15, 0.19).

Results and discussion

Molecular design and crystal structures

The bidentate phosphine ligands, dppb-Ac and dtpb-Ac, were synthesized through a similar three-step process with respective overall yields of 50% and 38%, as depicted in Fig. S1. The copper(I)–bromine clusters were facilely prepared by reacting CuBr with one equivalent of the corresponding bisphosphine ligand in dichloromethane. Single crystals suitable for X-ray analysis were obtained by diffusing diethyl ether into their filtered dichloromethane solutions. Impressively, these copper(I)–bromine clusters not only exhibit good solubility in various solvents but also demonstrate excellent sublimability. Thermal gravimetric analysis (TGA) and differential scanning calorimetry (DSC) conducted under a nitrogen atmosphere indicated that $[dppb-Ac]_2Cu_2Br_2$ and $[dtpb-Ac]_2Cu_2Br_2$ possess high decomposition temperatures (T_d) of 425 and 405 °C and high glass transition temperatures (T_g) of 175 and 138 °C, respectively (Fig. S6). The excellent processability and stability make them stand out among copper-halide clusters, particularly when it comes to purification *via* thermal gradient sublimation and device fabrication through either vacuum thermal deposition or solution processing. Both newly synthesized clusters were purified through successive recrystallization and

sublimation prior to characterization and device fabrication. The molecular structures of [dppb-Ac]$_2$Cu$_2$Br$_2$ and [dtpb-Ac]$_2$-Cu$_2$Br$_2$ were confirmed using ^{1}H-NMR,^{13}C-NMR, elemental analysis, and single-crystal X-ray diffraction analysis (CCDC numbers: 2386729 and 2386762). Detailed synthesis procedures and characterization data are provided in the SI.

Single-crystal X-ray diffraction analysis revealed distinct configurations of the two copper(I)–bromine clusters (Fig. 2a). [dppb-Ac]$_2$Cu$_2$Br$_2$ exhibited a butterfly-shaped Cu$_2$Br$_2$ core, with the copper(I) metal centers positioned in close proximity to each other ($d_{Cu–Cu}$ = 2.85 Å). The butterfly geometry indicates that the four-membered Cu$_2$Br$_2$ ring is folded along the Cu···Cu axis. These configuration characteristics resemble those of the previously reported copper(I)–halide clusters.[15] In comparison, when coordinated by the *ortho*-methylated bisphosphine ligand dtpb-Ac, [dtpb-Ac]$_2$Cu$_2$Br$_2$ adopted a symmetric parallelogram Cu$_2$Br$_2$ core (with the sum of the interior angles being 360°), and the Cu–Cu distance was significantly elongated to 3.10 Å. Each copper(I) atom in these clusters adopted a four-coordinate, tetrahedral-like configuration. The dimethylacridine donor units are nearly orthogonally attached to the bisphosphine ligands, with D–A dihedral angles of 85.63° in [dppb-Ac]$_2$Cu$_2$Br$_2$ and 81.76° in [dtpb-Ac]$_2$Cu$_2$Br$_2$. Besides the molecular configuration, the molecular packings of the copper(I)–bromine clusters are also influenced by *ortho*-methylation on the bisphosphine ligand. As depicted in Fig. 2c, [dppb-Ac]$_2$Cu$_2$Br$_2$ molecules are densely packed in the crystal lattice, with abundant intermolecular interactions among neighbouring molecules. In contrast, fewer and weaker intermolecular interactions are observed in the crystal lattice of [dtpb-Ac]$_2$Cu$_2$Br$_2$. Compared with [dppb-Ac]$_2$Cu$_2$Br$_2$, the significantly increased intermolecular distance between neighbouring [dtpb-Ac]$_2$Cu$_2$-Br$_2$ molecules is expected to more effectively inhibit emission quenching in aggregate states by avoiding short-distance Dexter energy transfer (DET).[16]
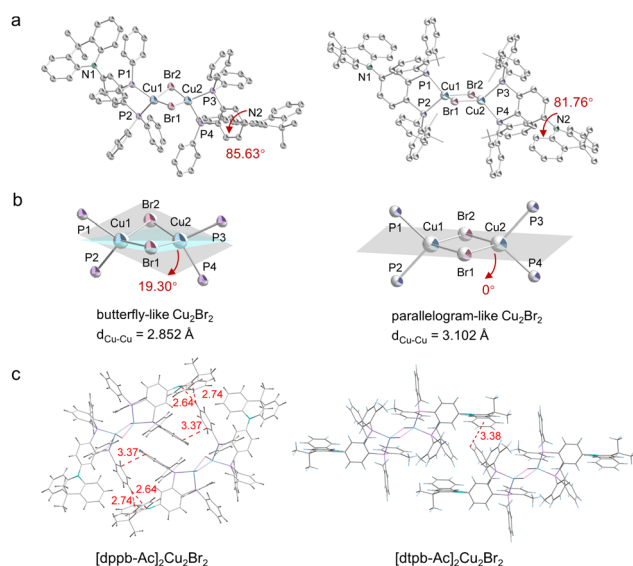
Theoretical calculations

To elucidate the characteristics of the frontier molecular orbitals (FMOs) and excited states of these copper(I)-bromine clusters, we performed density functional theory (DFT) and time-dependent DFT (TD-DFT) calculations using the B3LYP functional and 6-31G* basis set implemented in Gaussian. The highest occupied molecular orbitals (HOMOs) of both clusters are primarily localized on the Cu$_2$Br$_2$ cores with partial extension to the P atoms of the bisphosphine ligands, while the lowest unoccupied molecular orbitals (LUMOs) are mainly distributed over the central phenyl ring of the ligands (Fig. 3). The pronounced spatial separation between the HOMO and LUMO is expected to result in small ΔE_{ST} values for these copper(I)-bromine clusters. TD-DFT calculations revealed that the S$_1$ state of [dppb-Ac]$_2$Cu$_2$Br$_2$ is primarily characterized by a (metal + halogen)-to-ligand charge transfer [(M + X)LCT] transition (53%), along with a significant intra-ligand charge transfer (ILCT) component (46%) from the P atoms to the central phenyl rings of the ligands. In comparison, the contributions of the (M + X)LCT and *P*-to-phenyl ILCT transitions in the S$_1$ state of [dtpb-Ac]$_2$Cu$_2$Br$_2$ decrease to 42% and 40%, respectively, accompanied by a significantly increased ILCT transition (18%) originating from the dimethylacridine units to the central phenyl rings (Fig. 3 and Tables S7, S9). Replacing the partial (M + X)LCT transition with a dominant ILCT character in the emissive state may help suppress nonradiative Jahn–Teller distortions, which are commonly observed in the excited states of d^{10} metal complexes.[17] To gain further insight into the effects of *ortho*-methylation on the excited-state geometries, the root-mean-square displacements (RMSDs) between the optimized S$_0$ and S$_1$ geometries were calculated to quantify structural changes upon excitation. As depicted in Fig. 3, [dppb-Ac]$_2$Cu$_2$-Br$_2$ exhibits pronounced intramolecular motions, such as

Fig. 2 (a) Single-crystal structures; (b) configurations of the Cu$_2$Br$_2$ cores; (c) molecular packing diagrams.
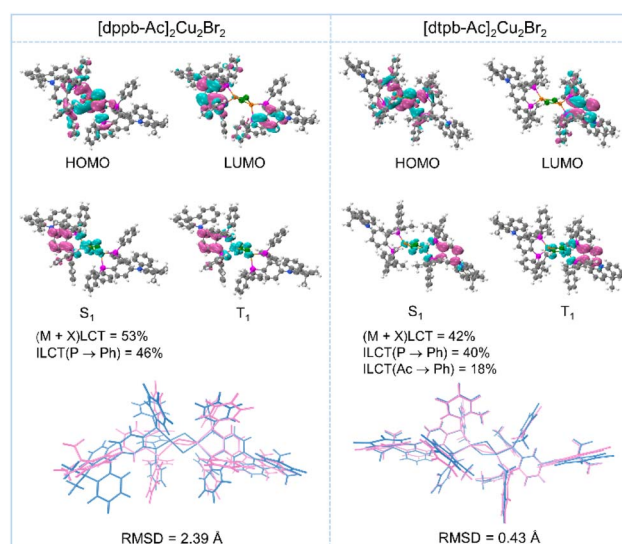

Fig. 3 (Upper) Frontier molecular orbital distributions, (middle) calculated excited-state properties, and (bottom) geometry comparison between S$_0$ (pink) and S$_1$ (blue) states of [dppb-Ac]$_2$Cu$_2$Br$_2$ and [dtpb-Ac]$_2$Cu$_2$Br$_2$.

rotations and twisting, resulting in poor overlap between the S_0 (pink) and S_1 (blue) geometries and a large RMSD value of 2.39 Å. In contrast, *ortho*-methylation on the bisphosphine ligand effectively restricts structural relaxation, yielding a markedly smaller RMSD of 0.43 Å for $[dtpb-Ac]_2Cu_2Br_2$. The effectively restricted excited-state relaxation is expected to contribute to the significantly higher emission efficiencies and narrower-band emission of $[dtpb-Ac]_2Cu_2Br_2$ in both solution and film states (*infra vide*).

Photophysical properties

The photophysical properties of both the clusters and the bisphosphine ligands were initially examined in dilute solutions.

As shown in Fig. 4a, $[dppb-Ac]_2Cu_2Br_2$ and $[dtpb-Ac]_2Cu_2Br_2$ exhibit similar ultraviolet-visible (UV-vis) absorption profiles in dichloromethane ($c = 1 \times 10^{-5}$ M), featuring strong bands below 340 nm and a weak shoulder band above 340 nm. The high-energy bands (<340 nm), which also appear in the absorption spectra of the respective ligands, can be assigned to the spin-allowed $\pi-\pi*$ transitions localized at the bisphosphine ligands. According to theoretical calculations (Fig. 3 and Tables S6–S9), the low-energy shoulder bands (>340 nm) of both clusters likely stem from a combination of (M + X)LCT and ILCT transitions. In degassed solutions, the clusters $[dppb-Ac]_2Cu_2Br_2$ and $[dtpb-Ac]_2Cu_2Br_2$ exhibited yellow and red emissions, with spectral peaks at 574 and 552 nm and full widths at half
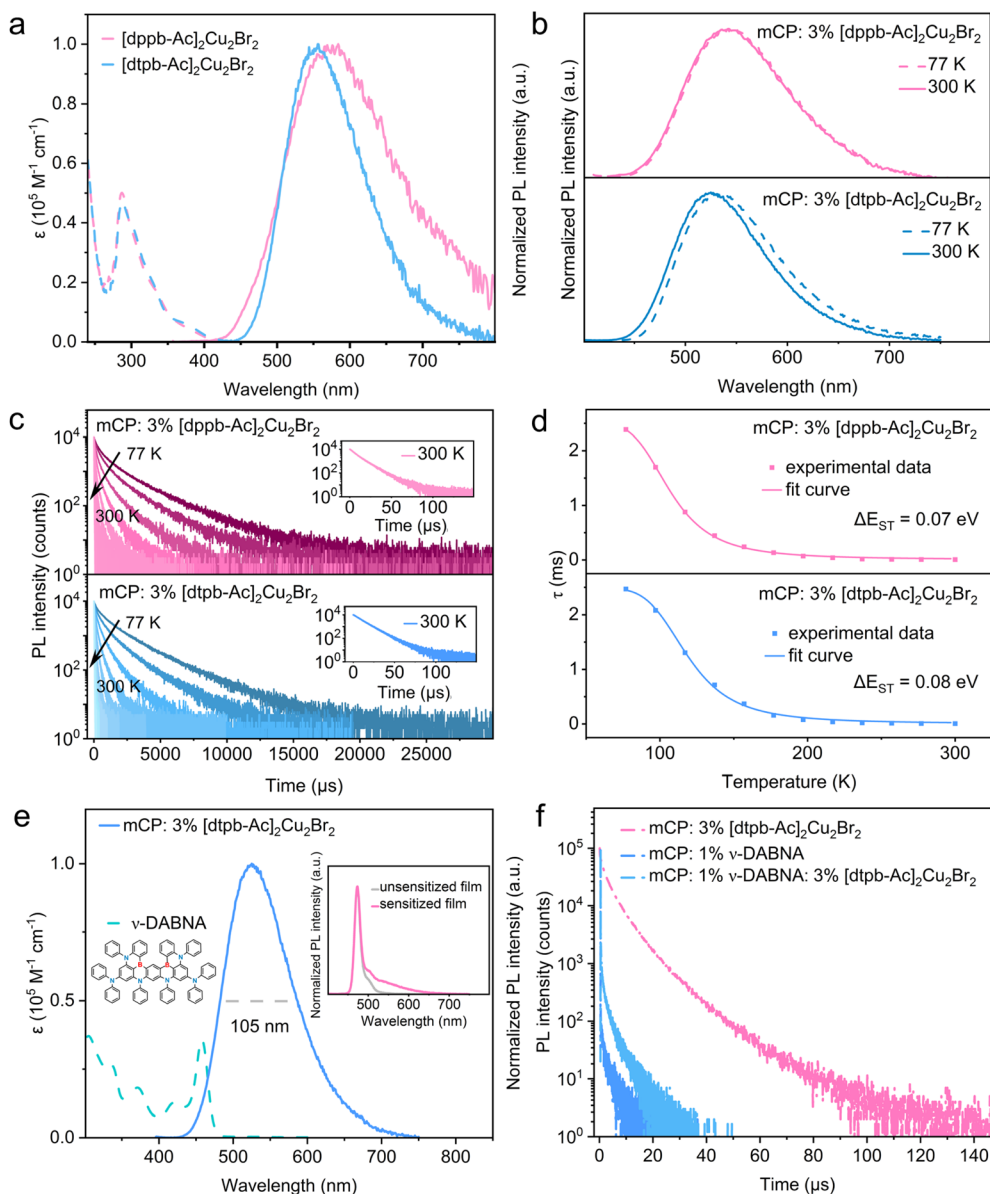
Fig. 4 a) Absorption and PL spectra in dichloromethane ($c = 10^{-5}$ M) at room temperature; (b) PL spectra in 3 wt%-doped mCP films; (c) PL decay curves in 3 wt%-doped mCP films from 77 to 300 K; (d) temperature dependence of the decay times in 3 wt%-doped mCP films; (e) absorption of *ν*-DABNA in dichloromethane ($c = 10^{-5}$ M) and PL spectra of $[dtpb-Ac]_2Cu_2Br_2$ in 3 wt%-doped mCP films. Inset: PL spectra of the unsensitized film (1 wt% *ν*-DABNA: mCP) and the sensitized film (1 wt% *ν*-DABNA: 3% $[dtpb-Ac]_2Cu_2Br_2$: mCP); (f) PL decay curves of the film samples.

maximum (FWHM) of 180 and 125 nm, respectively. Compared to [dppb-Ac]$_2$Cu$_2$Br$_2$, [dtpb-Ac]$_2$Cu$_2$Br$_2$ exhibits a significantly blue-shifted and narrower emission band (Fig. 4a). This is attributed to the deeper LUMO energy level, as revealed by cyclic voltammetry measurements (Fig. S7 and Table S5) and the suppressed excited-state structural deformation, as indicated by RMSD calculations (Fig. 3)—both resulting from the introduction of methyl groups onto the bisphosphine ligand. It is worth noting that no emission band from the ligand was observed, indicating that ligand dissociation in solution is effectively suppressed for both [dppb-Ac]$_2$Cu$_2$Br$_2$ and [dtpb-Ac]$_2$Cu$_2$Br$_2$.

We further investigated the photophysical properties of these two copper(I)-halide clusters dispersed in 1,3-bis(9-carbazolyl)benzene (mCP) films at a doping concentration of 3 wt%. The doped mCP films of [dppb-Ac]$_2$Cu$_2$Br$_2$ and [dtpb-Ac]$_2$Cu$_2$Br$_2$ exhibited bright yellow and green emissions at room temperature, with emission peaks at 540 and 525 nm, PLQYs of 65% and 99%, and decay times of 7.1 and 8.1 μs, respectively. The onset wavelengths of the room-temperature emission spectra of [dppb-Ac]$_2$Cu$_2$Br$_2$ and [dtpb-Ac]$_2$Cu$_2$Br$_2$ is very close, while the latter exhibited a much narrower emission profile. The similar emission onsets indicate nearly equal zero–zero energies (E_{0-0}) for the S$_1$ → S$_0$ transitions. The much narrower emission profile of [dtpb-Ac]$_2$Cu$_2$Br$_2$ compared with [dppb-Ac]$_2$Cu$_2$Br$_2$ is attributed to the effectively restricted excited-state distortion of the S$_1$ state through *ortho*-methylation, as revealed by the theoretical calculations (Fig. 3). To the best of our knowledge, near-unity PLQYs have rarely been reported for copper(I) emitters in evaporated films, due to non-radiative decay caused by their intrinsic excited-state distortions and/or poor sublimability.[18] As summarized in Table 1, [dppb-Ac]$_2$-Cu$_2$Br$_2$ and [dtpb-Ac]$_2$Cu$_2$Br$_2$ show comparable radiative rate constants ($k_r = \Phi_{PL}/\tau$) of 0.92 × 10^5 and 1.22 × 10^5 s^{-1}, respectively, while the nonradiative rate constant [$k_{nr} = (1 - \Phi_{PL})/\tau$] of the latter is only about one-fortieth of that of the former (0.12 × 10^4 *vs.* 4.93 × 10^4 s^{-1}). Consequently, the much higher PLQY of [dtpb-Ac]$_2$Cu$_2$Br$_2$ relative to [dppb-Ac]$_2$Cu$_2$Br$_2$ is primarily attributed to the effective suppression of nonradiative transitions by *ortho*-methylation on the bisphosphine ligands. Severe nonradiative decay, often driven by structural distortion from a tetrahedral-like ground state (d^{10}, sp^3) to a flattened excited state (d^9, dsp^2) upon photoexcitation, is a well-known challenge in achieving high emission efficiency in copper(I) complexes. The *ortho*-methyl groups effectively inhibit such excited-state deformations, as supported by theoretical calculations (Fig. 3). The temperature dependence of the emission spectra and decay times was studied for the copper(I)-halide clusters to elucidate the luminescence mechanism. As shown in

Fig. 4b, when the temperature decreased from 300 to 77 K, the emission spectra of [dppb-Ac]$_2$Cu$_2$Br$_2$ and [dtpb-Ac]$_2$Cu$_2$Br$_2$ exhibited a slight redshift. From the onset wavelength of the emission spectra at 300 and 77 K, the S$_1$ and T$_1$ energies and ΔE_{ST}s were calculated to be 2.73, 2.70 and 0.03 eV for [dppb-Ac]$_2$Cu$_2$Br$_2$, 2.77, 2.72 and 0.05 eV for [dtpb-Ac]$_2$Cu$_2$Br$_2$, respectively (Table 1). The decay times of [dppb-Ac]$_2$Cu$_2$Br$_2$ and [dtpb-Ac]$_2$Cu$_2$Br$_2$ increased several hundredfold, from 7.1 and 8.1 μs to 2.39 and 2.47 ms, respectively. These observations suggest that their emissions may originate from two excited states in fast thermal equilibrium, S$_1$ and T$_1$, with an energy spacing of ΔE_{ST}. In this case, the temperature dependence of the emission decay time (τ) can be described by the following Boltzmann equation:[6b,7,19]

$$\tau = \frac{3 + \exp\left(-\dfrac{\Delta E_{ST}}{k_B T}\right)}{\dfrac{3}{\tau_{T_1}} + \dfrac{1}{\tau_{S_1}}\exp\left(-\dfrac{\Delta E_{ST}}{k_B T}\right)} \quad (1)$$

Here, k_B denotes the Boltzmann constant and absolute temperature, respectively. As shown in Fig. 3d, the measured emission decay times at different temperatures from 77 to 300 K were well fitted using eqn (1), obtaining τ_{T1} values of 2.38 and 2.45 ms and 0.068 for [dtpb-Ac]$_2$Cu$_2$Br$_2$ and 0.078 eV for [dppb-Ac]$_2$Cu$_2$Br$_2$ and [dtpb-Ac]$_2$Cu$_2$Br$_2$, respectively. The τ_{T1} values are in good agreement with the decay times experimentally measured at 77 K, and the ΔE_{ST} values align well with the energy differences between the onsets of emission spectra recorded at 77 and 300 K (Fig. 4d and Table 1). These results confirm that the emissions of both copper(I)-halide clusters arise from the two thermally equilibrated excited states with closely similar energies. With increasing temperature from 77 to 300 K, triplet excitons become increasingly prone to thermal activation to the S$_1$ state, resulting in singlet emission. Owing to fast ISC and reverse ISC processes, the room-temperature emissions of these copper(I)-halide clusters are attributed to TADF.

Electroluminescent properties

To evaluate the EL performance of the two clusters, OLEDs with [dppb-Ac]$_2$Cu$_2$Br$_2$ and [dtpb-Ac]$_2$Cu$_2$Br$_2$ as terminal emitters were fabricated using the following device configuration: ITO/HAT-CN (10 nm)/TAPC (40 nm)/mCP (5 nm)/undoped emitter or an *x* wt% emitter doped in mCP (30 nm)/PPF (5 nm)/TmPyPB (35 nm)/Liq (1 nm)/Al (100 nm) (*x* = 3, 5, 15 and 25). Here, HAT-CN, TAPC, PPF, TmPyPB, and Liq served as the hole-injecting, hole-transporting, hole-blocking, electron-transporting, and electron-injecting layers, respectively. mCP, with a high triplet

Table 1 Photophysical data of the copper(I) clusters in 3 wt%-doped mCP films at 300 K

Compound	$\lambda_{PL}{}^a$, nm	$\Phi_{PL}{}^b$, %	τ^c, μs	$k_r{}^d$, 10^5 s^{-1}	$k_{nr}{}^e$, 10^4 s^{-1}	S$_1$/T$_1$/$\Delta E_{ST}{}^f$, eV
[dppb-Ac]$_2$Cu$_2$Br$_2$	540	65	7.1	0.92	4.93	2.73/2.70/0.03
[dtpb-Ac]$_2$Cu$_2$Br$_2$	525	99	8.1	1.22	0.12	2.77/2.72/0.05

a PL peak. *b* Photoluminescence quantum yield. *c* Emission decay time. *d* Radiative decay rate. *e* Nonradiative decay rate. *f* Energy levels and gap between the S$_1$ and T$_1$ states determined from the emission spectra at 77 and 300 K.
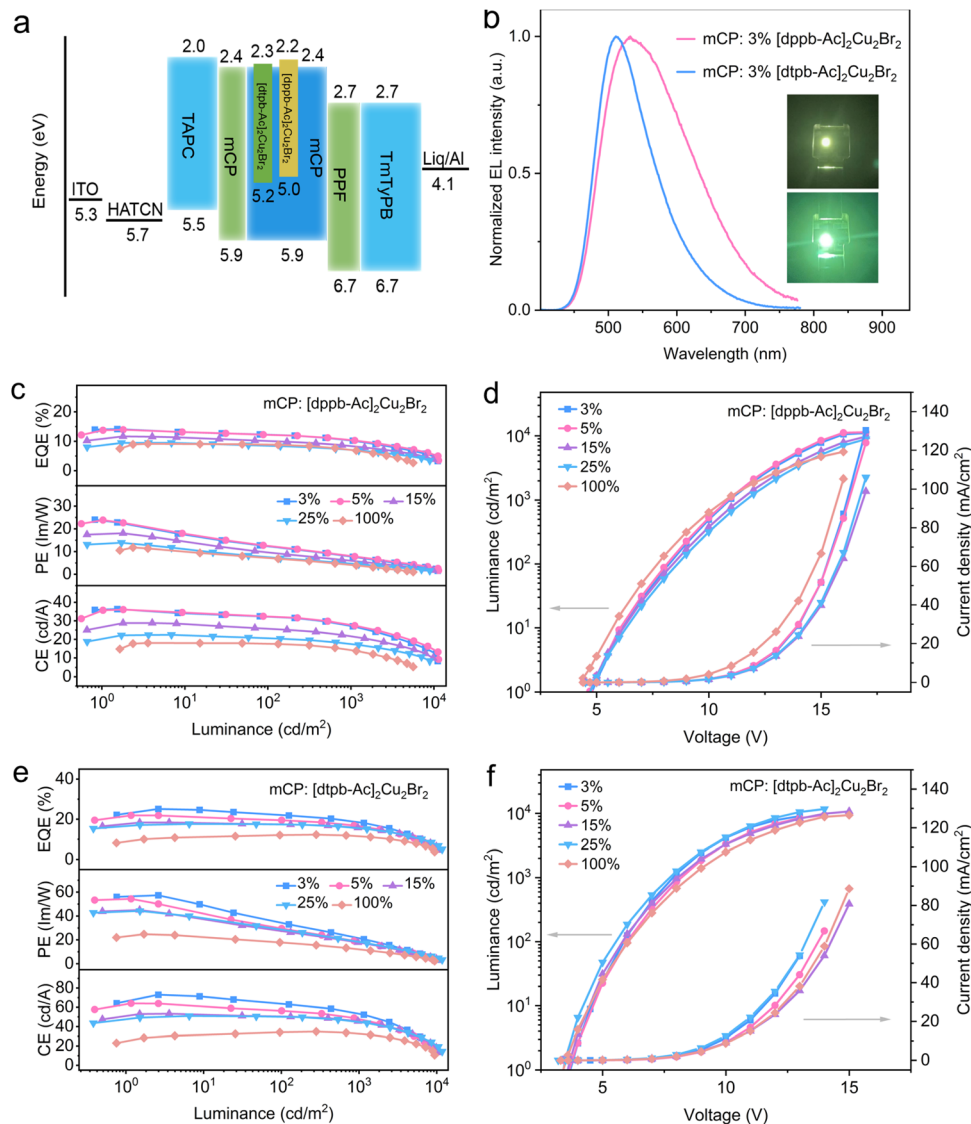
Fig. 5 OLEDs based on [dppb-Ac]$_2$Cu$_2$Br$_2$ and [dtpb-Ac]$_2$Cu$_2$Br$_2$ terminal emitters at various doping concentrations: (a) energy level diagram of the OLEDs; (b) EL spectra of 3 wt%-doped OLEDs; (c) and (e) external quantum efficiency (EQE), power efficiency (PE) and current efficiency (CE) vs. luminance characteristics; (d) and (f) density–voltage–luminance characteristics.

energy ($T_1 = 2.9$ eV), was selected as both the electron-blocking and host material to confine carriers within the emitting layer and ensure efficient exothermic energy transfer from the host to the emitter. The energy level diagram of these devices is shown in Fig. 5a, while the molecular structures of the organic materials are presented in Fig. S18. The device performance was investigated at emitter concentrations of 3%, 5%, 15%, 25%, and 100%. Graphical and numerical data illustrating the device performance are shown in Fig. 5 and Table 2, respectively.

A progressive redshift and broadening of the EL spectra were observed in the OLEDs based on both clusters as the emitter concentration increased (Table 2). For [dppb-Ac]$_2$Cu$_2$Br$_2$, the emission peaks shifted from 534 to 597 nm, with the FWHM increasing from 145 to 165 nm. Similarly, for [dtpb-Ac]$_2$Cu$_2$Br$_2$, the emission peaks shifted from 510 to 535 nm and the FWHM increased from 95 to 125 nm as the emitter concentration

increased from 3 to 100 wt%. These observations can be attributed to the solid solvation effect, which is common in CT-type emitters.[20] At high concentrations, the emissive CT states tend to be stabilized by the highly polar neighbouring molecules. The FWHM values of [dtpb-Ac]$_2$Cu$_2$Br$_2$-based devices are much lower than those of the [dppb-Ac]$_2$Cu$_2$Br$_2$-based devices, primarily due to the effective suppression of excited-state vibrational relaxation through the ortho-methylation strategy. The current density–voltage–luminance characteristics are shown Fig. 5d and f, revealing turn-on voltages of 4.8–4.4 V and maximum luminance of 11 370–5616 cd m^{-2} for [dppb-Ac]$_2$-Cu$_2$Br$_2$-based OLEDs and turn-on voltages of 3.7–3.4 V with a maximum luminance of 11 710–9053 m^{-2} for [dtpb-Ac]$_2$Cu$_2$-Br$_2$-based OLEDs. The efficiency–luminance curves are shown in Fig. 5c and e. Benefiting from the much higher PLQY of [dtpb-Ac]$_2$Cu$_2$Br$_2$ compared to [dppb-Ac]$_2$Cu$_2$Br$_2$, the 3 wt%-

Table 2 Performance of OLEDs employing the copper(I) clusters as terminal emitters

Emitter	Conc.[a], wt%	V_{on}[b], V	EQE$_{max}$[c], %	Roll-off[d], %	L_{max}[e], cd m^{-2}	CE[f], cd A^{-1}	PE[g], lm W^{-1}	λ_{EL}/FWHM[h], nm	CIE[i], (x, y)
[dppb-Ac]$_2$Cu$_2$Br$_2$	3	4.8	14.1/10.3	27.2	11 070	36.3	22.8	534/145	(0.38, 0.52)
	5	4.7	14/10.4	25	11 370	36.1	23.9	535/145	(0.38, 0.51)
	15	4.7	11.7/8.4	27.8	9763	28.8	18.1	545/156	(0.40, 0.51)
	25	4.6	9.5/7.1	25	8885	22.4	13.9	552/165	(0.42, 0.51)
	100	4.4	9.2/7.1	22.3	5616	18.1	11.8	597/162	(0.48, 0.48)
[dtpb-Ac]$_2$Cu$_2$Br$_2$	3	3.7	25.1/18.6	26	9053	73	57.4	510/95	(0.29, 0.52)
	5	3.6	21.9/16.6	24.1	9378	64.1	54.4	513/95	(0.29, 0.52)
	15	3.5	18.4/15.7	14.4	10 720	53	45	515/106	(0.32, 0.53)
	25	3.4	17.6/15.6	11.5	11 710	50.9	44.3	518/109	(0.33, 0.53)
	100	3.4	12.3/11.6	6	9381	34.8	24.8	535/125	(0.38, 0.54)

[a] Doping concentration. [b] Turn-on voltage at 1 cd m^{-2}. [c] Maximum EQE. [d] Efficiency roll-off at 1000 cd m^{-2}. [e] Maximum luminance. [f] Maximum current efficiency. [g] Maximum power efficiency. [h] EL peak and half-peak width at 1000 cd m^{-2}. [i] Commission Internatinale de L'Eclairage coordinates measured at 1000 cd m^{-2}.

doped device with the former as the emitter exhibited a significantly higher EQE$_{max}$ of 25.1%, which remained at 18.6% at 1000 cd m^{-2}. In contrast, the device with [dppb-Ac]$_2$Cu$_2$Br$_2$ showed a relatively lower EQE$_{max}$ of 14.1%, retaining 10.3% at 1000 cd m^{-2}. In addition, a high maximum current efficiency (CE$_{max}$) and power efficiency (PE$_{max}$) of 73 cd A^{-1} and 57.4 lm W^{-1} were achieved for the 3 wt%-doped device based on [dtpb-Ac]$_2$Cu$_2$Br$_2$. To the best of knowledge, the EL efficiency values of [dtpb-Ac]$_2$Cu$_2$Br$_2$ are among the highest reported for copper(I) emitters (Fig. 6f). As the emitter concentration increased, the device efficiencies of both clusters gradually decreased. Interestingly, compared to [dppb-Ac]$_2$Cu$_2$Br$_2$-based devices, [dtpb-Ac]$_2$Cu$_2$Br$_2$-based OLEDs exhibited a much more pronounced decrease in efficiency roll-off with increasing emitter concentration. For instance, the non-doped OLED of [dtpb-Ac]$_2$Cu$_2$Br$_2$ exhibited an EQE$_{max}$ of 12.3% and retained an EQE of 11.6% at 1000 cd m^{-2}, corresponding to a very small efficiency roll-off of 6%, which is much smaller than the 22.3% roll-off observed in the non-doped device of [dppb-Ac]$_2$Cu$_2$Br$_2$. This is partially attributed to the more effectively separated adjacent molecules in the aggregate state of [dtpb-Ac]$_2$Cu$_2$Br$_2$, as revealed by the crystal packing (Fig. 2c).

Although the OLEDs employing [dtpb-Ac]$_2$Cu$_2$Br$_2$ as the emitter exhibited outstanding efficiencies compared to previously reported copper(I) complexes, their emission spectra are very broad—a common shortcoming of copper(I) emitters featuring charge-transfer (CT)-type emissive states. The TADF-sensitized fluorescence (TSF) strategy, originally proposed by Duan[4a] and Adachi,[4b] utilizes D–A type TADF molecules as sensitizers for MR-TADF emitters and provides a promising route to simultaneously achieve high EL efficiency and excellent color purity. The efficiency of Förster resonance energy transfer (FRET) from the sensitizer to the emitter partially depends on the spectral overlap between the sensitizer's emission and the emitter's absorption. Although the emission spectra of [dtpb-Ac]$_2$Cu$_2$Br$_2$ in the doped films peak is at above 525 nm, the high-energy edge extends below 430 nm due to the broad spectral width (Fig. 4e). This unique feature, combined with its high-efficiency and short-lived TADF emission, endows [dtpb-Ac]$_2$Cu$_2$Br$_2$ with potential as a sensitizer for blue MR-TADF emitters (Fig. 6a). For instance, as

shown in Fig. 4e, there is proper overlap between the absorption spectrum of the representative deep-blue MR-TADF emitter ν-DABNA and the PL spectrum of the sensitizer [dtpb-Ac]$_2$Cu$_2$Br$_2$. The ratio of the overlapping region relative to the total emission band of the copper(I) sensitizer was calculated to be 4.7% for [dtpb-Ac]$_2$Cu$_2$Br$_2$, indicating the possibility of FRET from the sensitizer to the emitter. To preliminarily evaluate the potential of [dtpb-Ac]$_2$Cu$_2$Br$_2$ as a sensitizer, the PL spectrum and PL decay curve of a 1 wt% ν-DABNA: 3 wt% [dtpb-Ac]$_2$Cu$_2$Br$_2$: mCP film (sensitized film) were measured and compared with those of a 3 wt% [dtpb-Ac]$_2$Cu$_2$Br$_2$: mCP film and a 1 wt% ν-DABNA: mCP film (unsensitized film). As shown in Fig. 4e, the sensitized film exhibited narrowband blue emission from ν-DABNA, with only minor emission from [dtpb-Ac]$_2$Cu$_2$Br$_2$. Additionally, compared with the unsensitized film, the sensitized film showed an increased delayed fluorescence ratio in the decay curve (Fig. 4f). These results suggest efficient energy transfer from the sensitizer to ν-DABNA. Using a previously reported method[21] (see the SI for details), the FRET rate (k_{FRET}) and efficiency (η_{FRET}) from the sensitizer [dtpb-Ac]$_2$Cu$_2$Br$_2$ to the terminal emitter ν-DABNA were estimated to be 3.63×10^5 s^{-1} and 74.8%, respectively. The Förster radius (R_{FRET}) was calculated to be 5.79 nm, while the donor–acceptor distance between [dtpb-Ac]$_2$Cu$_2$Br$_2$ and ν-DABNA was estimated to be 4.84 nm. Given these relatively large distances, it is reasonable to disregard short-range Dexter energy transfer and instead consider long-range FRET as a predominant contributor to the excited-state dynamics of the sensitization system. Encouraged by this finding, we further constructed copper(I)-sensitized-fluorescent OLEDs employing [dtpb-Ac]$_2$-Cu$_2$Br$_2$ as the sensitizer, ν-DABNA as the terminal dopant, and mCP as the host material. The vacuum deposited TSF device featured an optimized structure of ITO/HATCN (10 nm)/TAPC (40 nm)/mCP (5 nm)/1 wt% ν-DABNA: 3 wt% [dtpb-Ac]$_2$Cu$_2$Br$_2$: mCP (30 nm)/PPF (5 nm)/TmPyPB (35 nm)/Liq (1 nm)/Al (100 nm) (Fig. 6b). For comparison, two additional devices were fabricated and characterized: Device A, employing 3 wt% [dtpb-Ac]$_2$Cu$_2$Br$_2$ as the terminal emitter, and Device B, an unsensitized reference device with the structure ITO/HATCN (10 nm)/TAPC (40 nm)/mCP (5 nm)/1 wt% ν-DABNA:mCP (30 nm)/PPF (5 nm)/TmPyPB (35 nm)/Liq (1 nm)/Al (100 nm) (Fig. 6b). The device
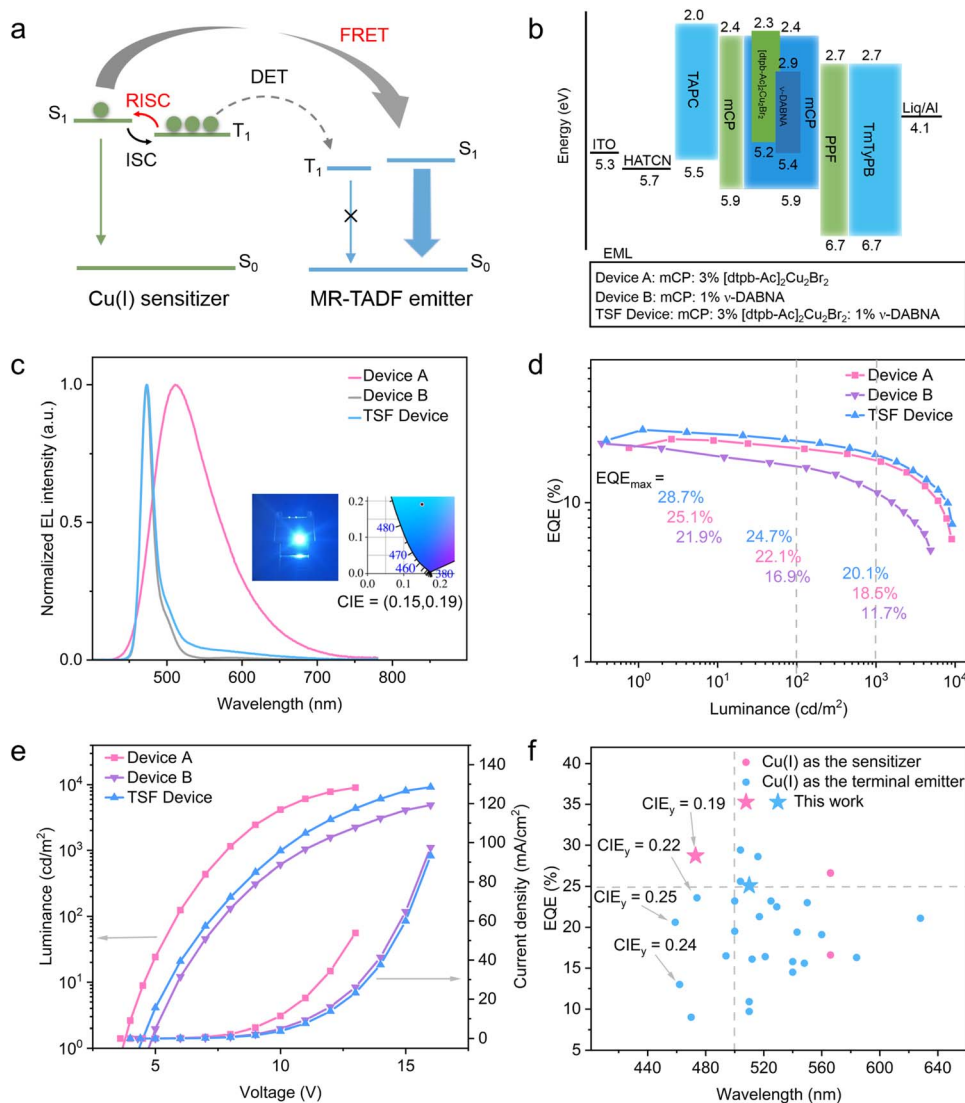
Fig. 6 (a) Schematic of the energy transfer mechanism for the copper(I) sensitized system; (b) energy level diagrams; (c) EL spectra; (d) EQE *versus* luminance curves; (e) current density–voltage–luminance characteristics; (f) EQE *versus* EL peak wavelength of representative copper(I) complex-based OLEDs.[6a,c,d,f,7b,14,15c,19,22]

performances are shown in Fig. 6c–e and Table 3. The TSF device achieved highly efficient blue emission, with CIE (x, y) coordinates of (0.15, 0.19). The EL spectrum of the TSF device closely resembled that of the unsensitized Device B, with both peaking at 473 nm and exhibiting nearly identical FWHMs of less than 19 nm (Fig. 6c), which differs significantly from the broad green emission of Device A. A slight low-energy tail observed in the EL spectrum of the TSF device is attributed to a minor emission

contribution from the sensitizer. With the assistance of the sensitizer, the TSF device exhibited a maximum external quantum efficiency (EQE_{max}) of 28.7%, an efficiency roll-off of 30.2% at 1000 cd m^{-2}, and a maximum luminance (L_{max}) of 9199 cd m^{-2}, all significantly superior to those of the unsensitized reference device (EQE_{max} = 22%, roll-off = 46.9%, and L_{max} = 4888 cd m^{-2}). These results suggest efficient FRET from the green-emissive copper(I) sensitizer to the deep-blue emitter ν-

Table 3 Performance of unsensitized and sensitized blue OLEDs

Device	$V_{on}{}^a$, V	EQE^b, %	Roll-off^c, %	$L_{max}{}^d$, cd m^{-2}	CE^e, cd A^{-1}	PE^f, lm W^{-1}	λ_{EL}/FWHM^g, nm	CIE^h, (x, y)
Device B	4.6	22/11.7	46.9	4888	20.1	12.6	473/18.5	(0.12, 0.14)
TSF device	4.3	28.7/20	30.2	9199	34.4	24.6	473/18.7	(0.15, 0.19)

^{a} Turn-on voltage at 1 cd m^{-2}. ^{b} EQE maximum value at 1000 cd m^{-2}. ^{c} Efficiency roll-off at 1000 cd m^{-2}. ^{d} Maximum luminance. ^{e} Maximum current efficiency. ^{f} Maximum power efficiency. ^{g} EL peak and half-peak width at 1000 cd m^{-2}. ^{h} Commission Internatinale de L'Eclairage coordinates measured at 1000 cd m^{-2}.

DABNA. To the best of our knowledge, this copper(I)-sensitized blue OLED not only ranks among the highest-efficiency OLEDs based on copper(I) complexes but also represents the first demonstration of deep-blue electroluminescence with EQE > 20% and CIE-y < 0.2 (Fig. 6f and Table S11).[6a,c,d,f,7b,14,15c,19,22]

Conclusions

In summary, we reported two sublimable TADF-emitting copper(I)-bromide clusters, [dppb-Ac]$_2$Cu$_2$Br$_2$ and [dtpb-Ac]$_2$Cu$_2$Br$_2$, coordinated by D–A type bisphosphine ligands. An *ortho*-methylation strategy was employed to modify the configuration of the Cu$_2$Br$_2$ cluster, thereby effectively suppressing nonradiative decay caused by excited-state distortions—a longstanding challenge in the design of high-efficiency copper(I) emitters. As a result, the optimized cluster [dtpb-Ac]$_2$Cu$_2$Br$_2$ exhibits green emission with a high PLQY of up to 99% in doped films, substantially higher than the PLQY of 65% observed for the control cluster [dppb-Ac]$_2$Cu$_2$Br$_2$. OLEDs doped with [dtpb-Ac]$_2$Cu$_2$Br$_2$ as the terminal emitter exhibited highly efficient green emission, achieving a high maximum EQE of 25.1% and a broad emission with a FWHM greater than 95 nm. Leveraging the high efficiency and broad emission of [dtpb-Ac]$_2$Cu$_2$Br$_2$, we successfully fabricated highly efficient green-sensitized deep-blue OLEDs by utilizing [dtpb-Ac]$_2$Cu$_2$Br$_2$ as the sensitizer for the blue MR-TADF emitter *v*-DABNA. The device achieved a maximum EQE reaching 28.7% and corresponding CIE coordinates of (0.15, 0.19). On the one hand, similar molecular design strategies are expected to be suitable for enhancing the emission efficiencies of copper(I) complexes in thin films by suppressing their intrinsic excited-state distortions. On the other hand, the broad emission spectra of copper(I) complexes—traditionally regarded as a limitation—can be harnessed as a beneficial feature to sensitize narrowband blue emitters, even when they exhibit green emission, thereby offering a new design strategy for copper(I)-based optoelectronic devices.

Author contributions

X. L. C. and J. M. L. conceived the project. X. L. and X. L. C. designed the experiments and analysed the data. X. L. performed sample preparation, OLED fabrication, and property measurements and drafted the initial manuscript. S. G. conducted theoretical calculations. X. L. (Xin Liu) assisted with synthesis and property measurements. Y. F. S. provided guidance on device fabrication. D. H. Z. contributed to data analysis. H. Y. assisted with single-crystal analysis. X. L. C. and J. M. L. revised the manuscript. All authors discussed and commented on the manuscript.

Conflicts of interest

The authors declare no conflict of interest.

Data availability

The data that support the findings of this study are available from the corresponding author upon reasonable request.

CCDC 2386729 and 2386762 contain the supplementary crystallographic data for this paper.[23a,b]

The data supporting this article are provided in the main manuscript and the supplementary information (SI). Supplementary information: general experimental information, detailed synthetic procedures, crystal structures, thermogravimetric analysis curves, electrochemical data, photophysical characterization, theoretical calculations, and device fabrication and characterization. See DOI: https://doi.org/10.1039/d5sc09307d.

Acknowledgements

Notes and references

1 (a) M. A. Baldo, D. F. O'Brien, A. You, A. Shoustikov, S. Sibley, M. E. Thompson and S. R. Forrest, *Nature*, 1998, **395**, 151–154; (b) H. Uoyama, K. Goushi, K. Shizu, H. Nomura and C. Adachi, *Nature*, 2012, **492**, 234–238; (c) Y. Liu, C. Li, Z. Ren, S. Yan and M. R. Bryce, *Nat. Rev. Mater.*, 2018, **3**, 18020.

2 (a) H. Fu, Y. M. Cheng, P. T. Chou and Y. Chi, *Mater. Today*, 2011, **14**, 472–479; (b) H. Yersin, A. F. Rausch, R. Czerwieniec, T. Hofbeck and T. Fischer, *Coord. Chem. Rev.*, 2011, **255**, 2622–2652.

3 T. Hatakeyama, K. Shiren, K. Nakajima, S. Nomura, S. Nakatsuka, K. Kinoshita, J. Ni, Y. Ono and T. Ikuta, *Adv. Mater.*, 2016, **28**, 2777–2781.

4 (a) D. Zhang, L. Duan, C. Li, Y. Li, H. Li, D. Zhang and Y. Qiu, *Adv. Mater.*, 2014, **26**, 5050–5055; (b) H. Nakanotani, T. Higuchi, T. Furukawa, K. Masui, K. Morimoto, M. Numata, H. Tanaka, Y. Sagara, T. Yasuda and C. Adachi, *Nat. Commun.*, 2014, **5**, 4016.

5 (a) C. Y. Chan, M. Tanaka, Y. T. Lee, Y. W. Wong, H. Nakanotani, T. Hatakeyama and C. Adachi, *Nat. Photonics*, 2021, **15**, 203–207; (b) S. O. Jeon, K. H. Lee, J. S. Kim, S. G. Ihn, Y. S. Chung, J. W. Kim, H. Lee, S. Kim, H. Choi and J. Y. Lee, *Nat. Photonics*, 2021, **15**, 208–215; (c) D. Zhang and L. Duan, *Nat. Photonics*, 2021, **15**, 173–174; (d) K. Stavrou, L. G. Franca, A. Danos and A. P. Monkman, *Nat. Photonics*, 2024, **18**, 554–561; (e) T. Hua, X. Cao, J. Miao, X. Yin, Z. Chen, Z. Huang and C. Yang, *Nat. Photonics*, 2024, **18**, 1161–1169; (f) H. Lee, R. Braveenth, S. Muruganantham, C. Y. Jeon, H. S. Lee and J. H. Kwon, *Nat. Commun.*, 2023, **14**, 419; (g) Z. Xiao, Y. Zou, Z. Chen, J. Miao, Y. Qiu, Z. Huang, X. Cao, X. Peng and C. Yang, *Adv. Mater.*, 2025, **37**, 2419601; (h) Y. Sun, X. F. Fu, C. L. Hou, T. T. Lin, D. H. Zhang, J. Liu, J. X. Hu, F. L. Lin, L. Zhou, L. Meng, X. L. Chen and C. Z. Lu, *Angew. Chem., Int. Ed.*, 2025, **64**, e202511921.

6 (a) M. Hashimoto, S. Igawa, M. Yashima, I. Kawata, M. Hoshino and M. Osawa, *J. Am. Chem. Soc.*, 2011, **133**, 10348–10351; (b) M. J. Leitl, V. A. Krylova, P. I. Djurovich, M. E. Thompson and H. Yersin, *J. Am. Chem. Soc.*, 2014, **136**, 16032–16038; (c) R. Hamze, J. L. Peltier, D. Sylvinson, M. Jung, J. Cardenas, R. Haiges, M. Soleilhavoup, R. Jazzar, P. I. Djurovich, G. Bertrand and R. E. Thompson, *Science*, 2019, **363**, 601–606; (d) S. Shi, M. C. Jung, C. Coburn, A. Tadle, M. R. D. Sylvinson, P. I. Djurovich, S. R. Forrest and M. E. Thompson, *J. Am. Chem. Soc.*, 2019, **141**, 3576–3588; (e) A. M. T. Muthig, O. Mrozek, T. Ferschke, M. Rodel, B. Ewald, J. Kuhnt, C. Lenczyk, J. Pflaum and A. Steffen, *J. Am. Chem. Soc.*, 2023, **145**, 4438–4449; (f) N. Zhang, L. Qu, S. Dai, G. Xie, C. Han, J. Zhang, R. Huo, H. Hu, Q. Chen, W. Huang and H. Xu, *Nat. Commun.*, 2023, **14**, 2901; (g) T. Y. Li, S. J. Zheng, P. I. Djurovich and M. E. Thompson, *Chem. Rev.*, 2024, **124**, 4332–4392.

7 (a) X. L. Chen, R. Yu, Q. K. Zhang, L. J. Zhou, X. Y. Wu, Q. Zhang and C. Z. Lu, *Chem. Mater.*, 2013, **25**, 3910–3920; (b) L. Zhan, A. Ying, Y. Qi, K. Wu, Y. Tang, Y. Tan, Y. Zou, G. Xie, S. Gong and C. Yang, *Adv. Funct. Mater.*, 2021, **31**, 2106345; (c) Y. Tan, A. Ying, J. Xie, G. Xie and S. Gong, *Chem. Sci.*, 2024, **15**, 11382–11390; (d) T. Y. Li, S. J. Zheng, P. I. Djurovich and M. E. Thompson, *Chem. Rev.*, 2024, **124**, 4332–4392.

8 (a) C. T. Cunningham, J. J. Moore, K. L. H. Cunningham, P. E. Fanwick and D. R. McMillin, *Inorg. Chem.*, 2000, **39**, 3638–3644; (b) M. Iwamura, S. Takeuchi and T. Tahara, *J. Am. Chem. Soc.*, 2007, **129**, 5248–5256.

9 H. Yersin and U. Monkowius, *Adv. Photonics Res.*, 2025, **6**, 2400111.

10 (a) X. Zhang and H. Xu, *Angew. Chem., Int. Ed.*, 2024, **63**, e202317597; (b) Y. Li, X. Zhang, Y. Man, S. Xu, J. Zhang, G. Zhang, S. Chen, C. Duan, C. Han and H. Xu, *Adv. Mater.*, 2023, **35**, e2302984; (c) X. L. Chen, R. Yu, X. Y. Wu, D. Liang, J. H. Jia and C. Z. Lu, *Chem. Commun.*, 2016, **52**, 6288–6291.

11 H. Yersin, R. Czerwieniec, M. Z. Shafikov and A. F. Suleymanova, *ChemPhysChem*, 2017, **18**, 3508–3535.

12 R. Czerwieniec, M. J. Leitl, H. H. H. Homeier and H. Yersin, *Coord. Chem. Rev.*, 2016, **325**, 2–28.

13 P. C. Ford, E. Cariati and J. Bourassa, *Chem. Rev.*, 1999, **99**, 3625–3647.

14 (a) M. Xie, C. Han, Q. Liang, J. Zhang, G. Xie and H. Xu, *Sci. Adv.*, 2019, **5**, eaav9857; (b) N. Zhang, H. Hu, L. Qu, R. Huo, J. Zhang, C. Duan, Y. Meng, C. Han and H. Xu, *J. Am. Chem. Soc.*, 2022, **144**, 6551–6557.

15 (a) A. Tsuboyama, K. Kuge, M. Furugori, S. Okada, M. Hoshino and M. Ueno, *Inorg. Chem.*, 2007, **46**, 1992–2001; (b) L. Kang, J. Chen, T. Teng, X. L. Chen, R. Yu and C. Z. Lu, *Dalton Trans.*, 2015, **44**, 11649–11659; (c) D. Volz, Y. Chen, M. Wallesch, R. Liu, C. Flechon, D. M. Zink, J. Friedrichs, H. Flugge, R. Steininger, J. Gottlicher, C. Heske, L. Weinhardt, S. Brase, F. So and T. Baumann, *Adv. Mater.*, 2015, **27**, 2538–2543.

16 (a) D. Zhang, X. Song, M. Cai and L. Duan, *Adv. Mater.*, 2018, **30**, 1705250; (b) H. Mubarok, A. Amin, T. Lee, J. Jung, J. H. Lee and M. H. Lee, *Angew. Chem., Int. Ed.*, 2023, **62**, e202306879.

17 J. H. Jia, D. Liang, R. Yu, X. L. Chen, L. Meng, J. F. Chang, J. Z. Liao, M. Yang, X. N. Li and C. Z. Lu, *Chem. Mater.*, 2019, **32**, 620–629.

18 R. Hamze, J. L. Peltier, D. Sylvinson, M. Jung, J. Cardenas, R. Haiges, M. Soleilhavoup, R. Jazzar, P. I. Djurovich, G. Bertrand and R. E. Thompson, *Science*, 2019, **363**, 601–606.

19 J. C. Deaton, S. C. Switalski, D. Y. Kondakov, R. H. Young, T. D. Pawlik, D. J. Giesen, S. B. Harkins, A. J. Miller, S. F. Mickenberg and J. C. Peters, *J. Am. Chem. Soc.*, 2010, **132**, 9499–9508.

20 (a) J. X. Hu, S. Jiang, D. H. Zhang, T. Zhao, F. L. Lin, L. Meng, X. L. Chen and C. Z. Lu, *Adv. Sci.*, 2023, **10**, 2300808; (b) X. L. Chen, X. D. Tao, Y. S. Wang, Z. Wei, L. Meng, D. H. Zhang, F. L. Lin and C. Z. Lu, *CCS Chem.*, 2023, **5**, 589–597.

21 Y. Y. Jing, N. Li, X. Cao, H. Wu, J. Miao, Z. Chen, M. Huang, X. Wang, Y. Hu, Y. Zou and C. Yang, *Sci. Adv.*, 2023, **9**, eadh8296.

22 (a) M. Osawa, M. Hoshino, M. Hashimoto, I. Kawata, S. Igawa and M. Yashima, *Dalton Trans.*, 2015, **44**, 8369–8378; (b) A. Verma, D. M. Zink, C. Fléchon, J. Leganés Carballo, H. Flügge, J. M. Navarro, T. Baumann and D. Volz, *Appl. Phys. A*, 2016, **122**, 191; (c) J. Zhang, C. Duan, C. Han, H. Yang, Y. Wei and H. Xu, *Adv. Mater.*, 2016, **28**, 5975–5979; (d) D. Di, A. S. Romanov, L. Yang, J. M. Richter, J. P. H. Rivett, S. Jones, T. H. Thomas, M. A. Jalebi, R. H. Friend, M. Linnolahti, M. Bochmann and D. Credgington, *Science*, 2017, **356**, 159–163; (e) X. Li, J. Zhang, Z. Zhao, X. Yu, P. Li, Y. Yao, Z. Liu, Q. Jin, Z. Bian, Z. Lu and C. Huang, *ACS Appl. Mater. Interfaces*, 2019, **11**, 3262–3270; (f) M. Klein, N. Rau, M. Wende, J. Sundermeyer, G. Cheng, C.-M. Che, A. Schinabeck and H. Yersin, *Chem. Mater.*, 2020, **32**, 10365–10382; (g) A. Ying, Y. H. Huang, C. H. Lu, Z. Chen, W. K. Lee, X. Zeng, T. Chen, X. Cao, C. C. Wu, S. Gong and C. Yang, *ACS Appl. Mater. Interfaces*, 2021, **13**, 13478–13486; (h) Q. Gu, F. Chotard, J. Eng, A. M. Reponen, I. J. Vitorica-Yrezabal, A. W. Woodward, T. J. Penfold, D. Credgington, M. Bochmann and A. S. Romanov, *Chem. Mater.*, 2022, **34**, 7526–7542; (i) A. Ruduss, B. Turovska, S. Belyakov, K. A. Stucere, A. Vembris, G. Baryshnikov, H. Agren, J. C. Lu, W. H. Lin, C. H. Chang and K. Traskovskis, *ACS Appl. Mater. Interfaces*, 2022, **14**, 15478–15493; (j) R. Tang, S. Xu, T. L. Lam, G. Cheng, L. Du, Q. Wan, J. Yang, F. F. Hung, K. H. Low, D. L. Phillips and C. M. Che, *Angew. Chem., Int. Ed.*, 2022, **61**, e202203982; (k) Y. Li, S. Xu, X. Zhang, Y. Man, J. Zhang, G. Zhang, S. Chen, C. Duan, C. Han and H. Xu, *Angew. Chem., Int. Ed.*, 2023, **62**, e202308410; (l) H. J. Wang, Y. Liu, B. Yu, S. Q. Song, Y. X. Zheng, K. Liu, P. Chen, H. Wang, J. Jiang and T. Y. Li, *Angew. Chem., Int. Ed.*, 2023, **62**, e202217195; (m) N. Zhang, Y. Li, S. Han, Y. Wei, H. Hu, R. Huo, C. Duan, J. Zhang, C. Han, G. Xie and H. Xu, *Angew. Chem., Int. Ed.*, 2023, **62**, e202305018; (n) R. Li, A. Ying, Y. Tan, Y. Ai and S. Gong,

Chem.–Eur. J., 2024, **30**, e202400817; (*o*) J. J. Wang, L. Z. Feng, G. Shi, J. N. Yang, Y. D. Zhang, H. Xu, K. H. Song, T. Chen, G. Zhang, X. S. Zheng, F. Fan, Z. Xiao and H. B. Yao, *Nat. Photonics*, 2023, **18**, 200–206; (*p*) A. Ying, Y. Tan and S. Gong, *Adv. Opt. Mater.*, 2024, **12**, 230333; (*q*) Y. Tan,

A. Ying, Y. Liu, X. Cai, L. Zhan, Z. Bin, J. You, C. Li and S. Gong, *Chem. Eng. J.*, 2024, **487**, 150618.

23 (*a*) CCDC 2386729: Experimental Crystal Structure Determination, 2026, DOI: 10.5517/ccdc.csd.cc2l3l8l; (*b*) CCDC 2386762: Experimental Crystal Structure Determination, 2026, DOI: 10.5517/ccdc.csd.cc2l3mbp.